Pressure and entropy changes in the flow-braking region during magnetic field dipolarization

S. Dubyagin,[1] V. Sergeev,[1] S. Apatenkov,[1] V. Angelopoulos,[2] R. Nakamura,[3] J. McFadden,[4] D. Larson,[4] and J. Bonnell[4]

Received 30 April 2010; revised 11 June 2010; accepted 23 June 2010; published 13 October 2010.

[1] Changes in plasma moments and entropy during dipolarizations are studied using Time History of Events and Macroscale Interactions during Substorms observations made near the neutral sheet at 6–12 R_E on the nightside. Plasma tube entropy ($pV^{5/3}$) at the observation point is estimated for the data set of 147 dipolarizations using the formula of Wolf et al. (2006). Plasma pressure began to increase shortly before dipolarization and proceeded without considerable entropy change until the arrival of the dipolarization front, after which major entropy changes occurred. We have found that on average, postdipolarization plasma pressure changes very little from predipolarization plasma pressure at r = 10–12 R_E and increases only slightly in the near-Earth region. Although the associated plasma tube entropy always decreases in the region downtail of r = 8 R_E, this decrease becomes smaller closer to the Earth. The local entropy estimate $pn^{-5/3}$ shows a large increase, however, suggesting ~40% reduction in flux tube particle content after dipolarization. Our statistical results provide a constraint for dipolarization theories and support the bubble model of dipolarizations.

Citation: Dubyagin, S., V. Sergeev, S. Apatenkov, V. Angelopoulos, R. Nakamura, J. McFadden, D. Larson, and J. Bonnell (2010), Pressure and entropy changes in the flow-braking region during magnetic field dipolarization, *J. Geophys. Res.*, *115*, A10225, doi:10.1029/2010JA015625.

1. Introduction

[2] Dipolarization, a sudden increase in the magnetic field component B_z combined with a decrease in the radial B component, is a basic manifestation of substorm expansion in the near-Earth plasma sheet. It is generally believed to be associated with partial diversion of the crosstail current via the ionosphere in the limited longitudinal sector of the tail current sheet, that is, by the formation of the 3-D substorm current wedge (SCW) system [*McPherron et al.*, 1973].

[3] There are indications that current diversion and dipolarization sometimes start to develop in the near-Earth plasma sheet at distances <10 R_E [*Jacquey et al.*, 1991, 1993; *Ohtani et al.*, 1992], so they may not be directly related to the reconnection process developing farther downtail at ≥20 R_E [*Nagai et al.*, 1998; *Lui et al.*, 1998; *Miyashita et al.*, 2000]. Two competing substorm scenarios, current disruption (CD) [*Lui*, 1996] and near-Earth neutral line (NENL) [*Baker et al.*, 1996; *Shiokawa et al.*, 1998], propose different physical mechanisms for dipolarization. According to the CD scenario, current disruption results from development of current-driven instability in the near-Earth plasma sheet. The NENL model argues that interaction of plasma flows from the reconnection region with the dipole-like magnetic field may lead to SCW formation. As shown by *Shiokawa et al.* [1998] from observations and by *Birn et al.* [1996] from MHD simulations, braking of longitudinally localized, high-speed plasma flows (bursty bulk flows, or BBFs) when they reach the dipole-like inner magnetosphere would lead to magnetic flux pileup and development of an SCW-like field-aligned current system.

[4] BBFs are of special interest when discussing dipolarizations. Those of a few minutes' duration, which are generally thought to be products of high-speed reconnection outflows, are observed in the plasma sheet for any activity level and provide a major contribution to Earthward magnetic flux transport [*Baumjohann et al.*, 1990; *Angelopoulos et al.*, 1994]. At any distance in the plasma sheet, a BBF carries a localized region of enhanced B_z with a sharp leading front, a "local dipolarization" [*Ohtani et al.*, 2004]; it is also likely to include field-aligned currents of SCW polarity [*Nakamura et al.*, 2001; *Birn et al.*, 2004]. Statistical plasma sheet BBFs are underpopulated flux tubes with reduced plasma pressure and density inside this local dipolarization [*Ohtani et al.*, 2004]. The large velocity of plasma sheet BBFs does not guarantee that they may easily penetrate the near-Earth inner region, as confirmed by dual satellite studies of BBF penetration [*Takada et al.*, 2006].

[1] Earth Physics Department, St. Petersburg State University, St. Petersburg, Russia.
[2] Institute of Geophysics and Planetary Physics, University of California, Los Angeles, California, USA.
[3] Space Research Institute, Austrian Academy of Sciences, Graz, Austria.
[4] Space Sciences Laboratory, University of California, Berkeley, California, USA.

0148-0227/10/2010JA015625

[5] As deduced from empirical models of the magnetotail, the radial profile of the plasma tube entropy parameter ($S = pV^{5/3}$, where $V = \int ds/B$ is the volume of a unit magnetic flux tube and p is plasma pressure) displays a significant decrease toward the Earth. This entropy reduction contradicts the ideal MHD prediction that entropy is conserved for a magnetic flux tube moving adiabatically along a convection streamline toward the Earth [*Erickson and Wolf*, 1980]. Moreover, with an entropy reduction profile, the inner magnetosphere tends to push out the higher-entropy plasma forced to flow inward, as confirmed by global MHD and Rice Convection Model (RCM) simulations [*Lemon et al.*, 2004].

[6] *Pontius and Wolf* [1990] suggested a theoretical model of BBFs based on interchange instability, which exploits and explains the entropy reduction profile. They proposed that some mechanism in the magnetotail creates localized flux tubes with reduced entropy, which they called "bubbles." These tubes become electrically polarized and move toward the Earth at high speed relative to neighboring tubes, which have higher entropy. The motion continues until the bubble entropy equals the entropy of ambient plasma. The plasma density or pressure depletion observed in the BBF core (where B_z is increased) provides strong observational evidence in favor of the bubble picture of BBFs [*Sergeev et al.*, 1996; *Ohtani et al.*, 2004], which has been confirmed in a number of simulations [*Lemon et al.*, 2004; *Birn et al.*, 2004] and was reviewed recently by *Wolf et al.* [2009] and *Birn et al.* [2009].

[7] The main purpose of our study is to explore how the plasma pressure and entropy change during dipolarizations and to study the role of the bubble scenario in Earthward plasma injection and dipolarization. Although a number of previous studies have been made of nightside dipolarizations in the distance range 6–12 R_E, covering the transition region between current sheet and dipole and the outer part of the dipole-like region [*Lopez and Lui*, 1990; *Ohtani et al.*, 1992; *Lui et al.*, 1992], they did not give a clear picture of pressure and entropy change in that region.

[8] In this work, we study the evolution of plasma parameters in the equatorial plane during a dipolarization using the excellent coverage and instrumentation of the Time History of Events and Macroscale Interactions during Substorms (THEMIS) probes (P1, P2, P3, P4, P5). There are four basic obstacles to understanding the pressure and entropy variations and deciding on the importance of the bubble mechanism in replenishing inner magnetospheric plasma. First, data from different plasma instruments covering both thermal and superthermal plasma sheet energies (hundreds of eV to hundreds of keV) must be combined to get a realistic total ion pressure in the inner region. In our case we combine observations from two THEMIS plasma spectrometers (electrostatic analyzer [ESA] and solid state telescope [SST]) to cover the required energy range.

[9] Second, during dipolarizations, severe local plasma sheet thinnings and thickenings distort plasma sheet geometry and contribute to plasma parameter variations. With a large number of dipolarization events measured by five THEMIS probes, we avoid complications by analyzing only observations made in the vicinity of the neutral sheet.

[10] Third, with fast flows, quickly changing magnetic field, and essential plasma dynamics along the flux tubes (as revealed in the bubble simulations [*Birn et al.*, 2004]), the constancy of plasma pressure along the field lines used in the computation of plasma tube entropy is no longer a good approximation. We try to avoid this difficulty by analyzing the postdipolarization state, when these problems should be considerably reduced.

[11] Fourth, estimation of the plasma tube volume V requires an adequate magnetospheric model to integrate along the magnetic field line. Having no simple method of constructing a model for every particular event, we evaluate flux tube entropy from spacecraft plasma and field measurements using the formula of *Wolf et al.* [2006], which is based on force-balanced Tsyganenko models.

[12] In addition, a statistical study of entropy evolution requires that general assumptions be made. Since the entropy must be conserved for a particular flux tube along a streamline, statistical results could be influenced by systematic variations in external conditions or by systematic changes in streamlines during dipolarization. Throughout the paper we assume that these variations are random and do not influence averaged results.

2. Observations

2.1. Data

[13] We use data from identical instruments on board THEMIS probes. The spin-averaged (~3 s) magnetic and electric field data come from the fluxgate magnetometer (*Auster et al.* [2008]) and the Electric Field Instrument (EFI, *Bonnell et al.* [2008]). We use spin plane electric field components (E_x, E_y GSE) after removing the offset to compute the third component from ($\mathbf{E} \cdot \mathbf{B}$) = 0; this procedure was used when the angle between the magnetic field vector and the spin plane was >15°.

[14] Particle data came from the ESA measuring ion and electron fluxes over energy ranges of 5–25,000 eV and 2–30,000 eV, respectively [*McFadden et al.*, 2008] and the SST, which measured ion fluxes from ~30 keV up to 6 MeV. The plasma pressure was computed as a sum of contributions from ESA ions and electrons and SST ions. We used calibration procedures from version 04 THEMIS software, including solar contamination removal for SST ion data.

[15] Here we use the sharp increases in B_z at a rate ≥1 nT/min and amplitude ≥5 nT to identify dipolarization (the events for our statistics were selected visually). The dipolarizations selected according to such criteria demonstrate a wide variety of characteristics. Two examples of dipolarizations observed by THEMIS P3 and characteristic epoch times (t_0, t_{0D}, t_{DIP}) are shown in Figure 1. Although the magnetic field component B_z increased by ~10 nT for 5–10 min in both cases, the initial conditions differed. The event on 17 January 2008 (Figure 1, left) was observed in the near-Earth region (r = 8.1 R_E) where the magnetic field configuration was already dipole-like ($B_z \sim 35$ nT) by the time of dipolarization onset, and plasma pressure was high, $P \sim 0.9$ nPa. The event on 23 January 2008 (Figure 1, right) took place in the initially stretched configuration with $B_z \sim 6$ nT and low plasma pressure ($P \sim 0.2$ nPa). Despite these differences, the manifestations of dipolarizations are similar. The onsets of sharp B_z variations (t_{0D}) occurred at 0051:30 UT (Figure 1, left) and 0339:20 UT (Figure 1, right). The B_z growth at 0051:30–0057:00 UT (Figure 1, left) and at 0339:20–0353:00 UT (Figure 1, right) was accompanied by irregular magnetic field

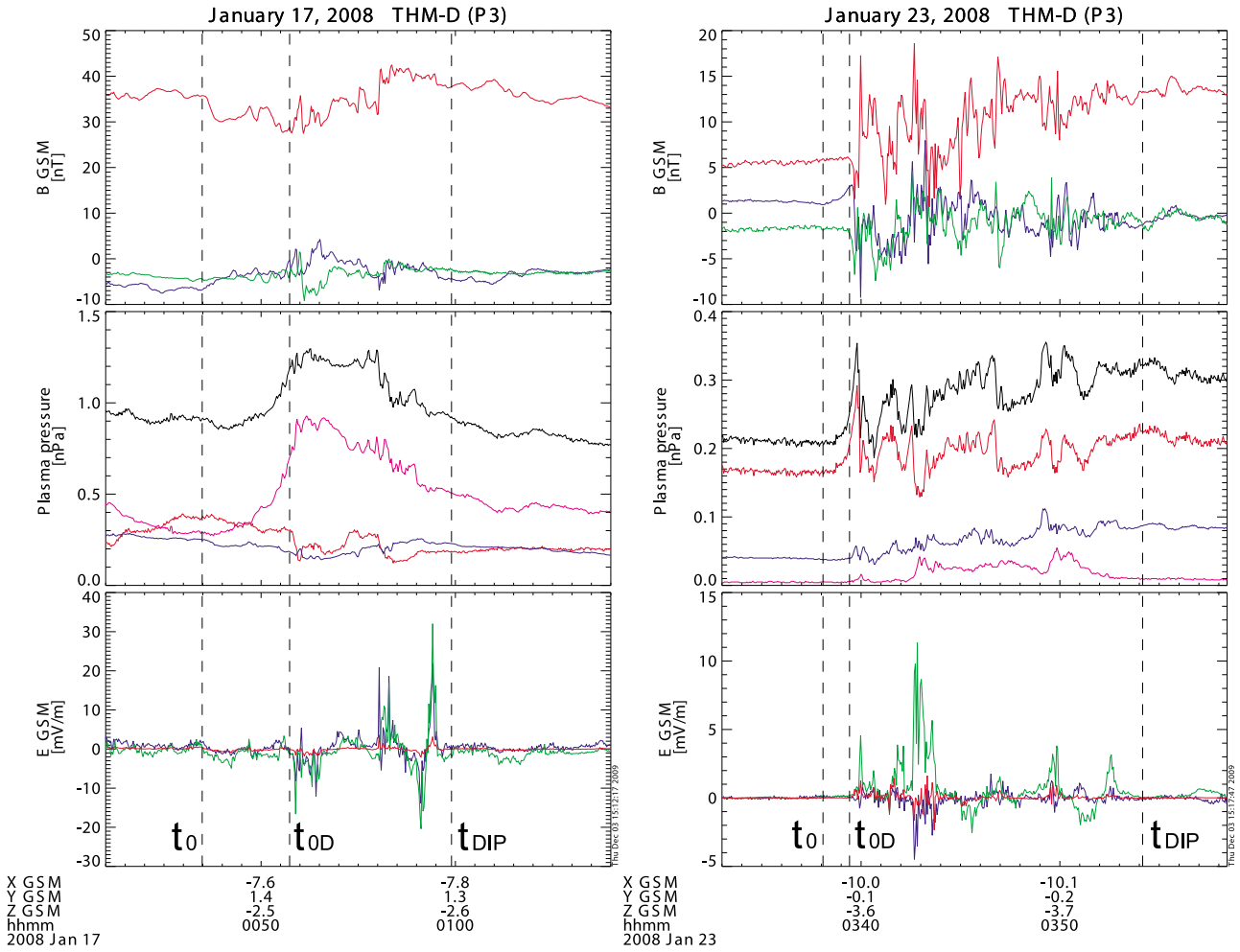

Figure 1. THEMIS P3 observations of dipolarizations: (top) magnetic field GSM X, Y, Z components (shown in blue, green, and red, respectively); (middle) plasma pressure (black curve) and contributions from different detectors (red, ESA ions; blue, ESA electrons; and magenta, SST ions); and (bottom) electric field GSM components. Vertical dashed lines indicate t_0, t_{0D}, and t_{DIP} times (see explanation in text).

perturbations with amplitude comparable to that of the final B_z increase. The perturbations were accompanied by short electric field bursts (Figure 1, bottom). Note that the 23 January event started with a sharp, short B_z drop (~0339:30 UT), and then B_z increased. Such B_z drops are observed frequently before dipolarization; their time scales range from a few seconds [*Runov et al.*, 2009] to a few minutes. By 0059:50 UT (Figure 1, left) and 0354:10 UT (Figure 1, right) the magnetic and electric field variations faded. The resultant postdipolarization state should be closer to the pressure equilibrium state than during the time period preceding the dipolarization.

[16] We emphasize that sharp, transient B_z and E_y variations are often preceded by smooth changes in the pressure and magnetic field. For example, the pressure started to increase 2 min before B_z onset for the 17 January event and 1 min before B_z onset for the 23 January event. Such precursors are observed in roughly half of all the events considered. This gradual pressure increase can be accompanied by slow magnetic field changes in B_x, B_y components (e.g., B_x increase in Figure 1 [right] between 0338:10 and 0339:20 UT). These variations are considered a precursor of a dipolarization. Accordingly, to study the effects of dipolarizations, we identify two onset times: the onset of sharp B_z variations (t_{0D}) and the onset of their precursors (t_0).

[17] The choice of timing requires additional comments. Depending on the probe mode, the full SST distribution (from which accurate plasma moment computation is possible) is available at 3 s or 3 min. In the latter case, to estimate moments at particular times we would need to interpolate between sparse SST measurements. Actually, t_0 can be taken slightly earlier and t_{DIP} slightly later without influencing the results of pre- and postdipolarization state comparisons. We made use of this fact to match these times with SST measurements when the full distribution function was available at low (3 min) resolution. To minimize the effect of probe motion, we tried to keep $\Delta t = t_{DIP} - t_0 \leq 20$ min. Furthermore, quick recovery of the plasma pressure after completion of dipolarization, as seen in Figure 1 (left) also constrains the choice of t_{DIP}. In the cases of recurrent dipolarizations, we required that the recovery interval with no fast perpendicular flows (as inferred from EFI data) be longer than 5 min. In those cases, we considered only the first dipolarization of a series.

2.2. Coordinate System and Event Selection Criteria

[18] In the plasma sheet, the relationship $\partial/\partial z \gg \partial/\partial x$ is often fulfilled, and plasma parameters are constant along the field line owing to isotropy of the ion distribution function. Hence, even small displacement along Z is equivalent (in terms of plasma parameters) to much greater displacement in the X direction. Therefore, when studying evolution of the parameters near the equatorial plane as functions of radial distance, we need also to control the distance of the probe from the neutral sheet. If the current sheet is parallel to the XY GSM plane, the proxy measure of this distance is B_x/B_z, which is zero at the neutral sheet plane. Actually the neutral sheet in the near-Earth region undergoes strong warping and tilting due to magnetic dipole tilt (the solar wind is also a factor [*Tsyganenko and Fairfield*, 2004]). At r = 6–12 R_E the magnetic field configuration displays more axial symmetry than a 2-D cartesian symmetry. In this case for each event we define a proper (neutral sheet-based) coordinate system using the empirical model of neutral sheet surface [*Tsyganenko and Fairfield*, 2004] as follows.

[19] For given epoch, solar wind conditions (OMNIWeb database, 1 h averaged), and probe coordinates, we start from a point of the model neutral sheet $\mathbf{r}_{\mathrm{NS}}$ nearest to the probe. A vector normal to the neutral sheet is computed for this point (pointing north), giving us the first coordinate vector $\mathbf{e}_z^{\mathrm{NS}}$. The second vector is defined as

$$\mathbf{e}_y^{\mathrm{NS}} = \frac{\mathbf{r}_{\mathrm{NS}} \times \mathbf{e}_z^{\mathrm{NS}}}{r_{\mathrm{NS}}}. \quad (1)$$

[20] The third vector is then $\mathbf{e}_x^{\mathrm{NS}} = \mathbf{e}_y^{\mathrm{NS}} \times \mathbf{e}_z^{\mathrm{NS}}$. For a plane current sheet and zero dipole tilt angle, $\mathbf{e}_x^{\mathrm{NS}}$, $\mathbf{e}_y^{\mathrm{NS}}$, and $\mathbf{e}_z^{\mathrm{NS}}$ coincide with $-\mathbf{e}_r^{\mathrm{GSM}}$, $-\mathbf{e}_\varphi^{\mathrm{GSM}}$, and $\mathbf{e}_z^{\mathrm{GSM}}$ of cylindrical GSM, respectively. Although this local coordinate system can be constructed for every point in the probe's trajectory, we determine it once for each event at the time of dipolarization onset (t_{0D}) and use it throughout the entire event.

[21] By examining visually the probe's magnetogram in the NS frame for each event, we selected those cases in which $|B_{x\mathrm{NS}}/B_{z\mathrm{NS}}| < 1$ for a few minutes both before and after dipolarization. This condition ensures that data were taken in the proximity of the neutral sheet on the field lines that crossed the neutral sheet surface not far from the probe.

[22] To minimize the effect of probe radial displacement during the event, we require that the time interval between t_0 and t_{DIP} be ≤20 min, so displacement is ≤0.5 R_E. However, both pressure and magnetic field in the near-Earth region grow very fast toward the Earth. For the dipole field $\partial B/\partial r \sim$ 30 nT/0.5 R_E at r = 6 R_E and ~2 nT/0.5 R_E at r = 12 R_E. Although for most events in our database the probes were near their apogee and radial displacement was less than 0.25 R_E in ~92% of events, possible effects of movement should be taken into account for inbound- or outbound-moving probes in the near-Earth part of a considered region. The thinner the current sheet, the lower the probability that the probes are near the neutral sheet. Thus, our limit imposed on $|B_{x\mathrm{NS}}/B_{z\mathrm{NS}}|$ is unfavorable to the selection of dipolarizations observed near very thin current sheets. We restrict our database events to be inside the sector ±3 h magnetic local time from midnight and in the geocentric distance range r = 6–12 R_E, which covers the area of potential flow braking of primary interest to us.

2.3. Statistical Properties of Dipolarizations

[23] In this study we surveyed THEMIS observations for the period between 12 December 2007 and 6 March 2008 and we found 147 events that met our criteria. The majority of events in our data set came from the near-Earth trio of probes, P3, P4, and P5 (71, 40, and 30 events); only a few events were recorded by P1 or P2 (1 and 5 events). Figure 2a shows the spatial distribution of dipolarizations in our data set. As one might expect from BBF statistics [*Angelopoulos et al.*, 1994], the majority of events were observed in the pre-midnight sector. To characterize the activity conditions, we use the maximum of the Kyoto preliminary auroral electrojet index AE over the $[t_0, t_{\mathrm{DIP}}]$ interval. As seen from Figure 2b, $AE_{\max}$ was less than 400 nT in 84% of events, and $AE_{\max}$ < 200 nT for 54%, demonstrating that, on average, activity was moderate. Note also that there were a significant number of events with $AE_{\max}$ < 100 nT.

[24] The magnetic field change after dipolarization can be characterized by $\Delta B_z = B_z^{(\mathrm{DIP})} - B_z^{(0)}$ (where the contribution of the Earth's dipole was subtracted from the total magnetic field to reduce the effect of probe movement). Figure 2c shows that the majority of dipolarizations in our data set are rather weak, with 69% having ΔB_z < 10 nT. It should be noted that peak values of ΔB_z during the turbulent dipolarization [$\Delta B_{z\max} = \max(B_z) - B_z^{(0)}$ shown in Figure 2d] are larger, especially at r > 9 R_E, and depend only slightly on r (Figure 1). The two most intense events with ΔB_z > 40 nT occur inside geosynchronous orbit.

2.4. Plasma Parameter Change

[25] The ion temperature is higher in the inner magnetotail than in the midtail plasma sheet. Moreover, dipolarizations are accompanied by acceleration of particles to higher energies. Considering the energy range of the THEMIS instruments, this means that the main contributors to the plasma pressure often transit from the ESA energy range to the SST energy range during dipolarization. Because the ion temperature in the plasma sheet is known to be a few times higher than the electron temperature [*Baumjohann*, 1993], the contribution to plasma pressure from SST electrons with energies >30 keV was neglected. Removal of the solar contamination from SST data is possible only if the full distribution function is available. Therefore, the plasma moments were computed from the reduced distribution functions measured by ESA (sampled at 3 s resolution) and from the full ion distribution function measured by SST (sampled at 3 s or 3 min resolution depending on instrument mode). It is assumed that pressure is isotropic and all ions are protons. We also neglected the ESA electron fluxes below the 30 eV energy limit to exclude the photoelectron contribution to pressure and density (the probe potential was less than 25 V for all events). For events in which full distribution of SST ions was available only at 3 min resolution, we used linear interpolation of SST data, synchronizing them with 3 s ESA cadence. Whenever possible, we tried to match t_0 and t_{DIP} with times of SST measurements as described in section 2.1.

[26] P_{DIP} and P_0 values are measured at different locations in space. To correct for probe motion, we need to know

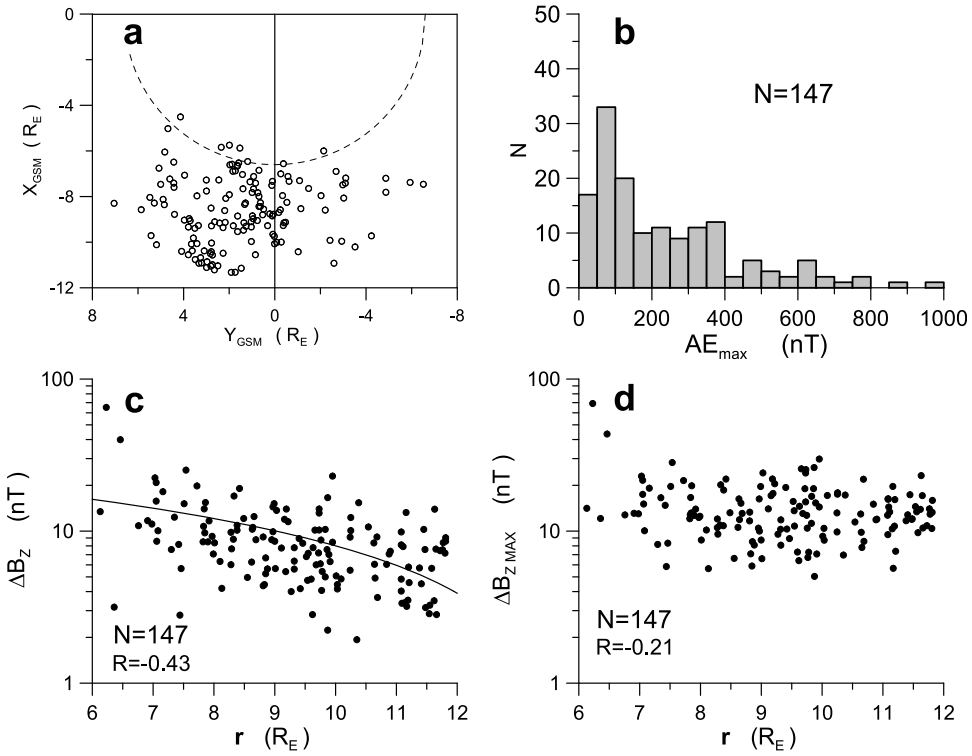

Figure 2. (a) Distribution of dipolarization events in the *XY* GSM plane. The dashed semicircle represents geostationary orbit. (b) The histogram of maximal *AE* during the dipolarization period. (c) The amplitude of dipolarization $\Delta B_z = B_z^{(DIP)} - B_z^{(0)}$ versus geocentric distance on a logarithmic scale. (d) The same as Figure 2c but for maximal (peak) dipolarization amplitude. The solid line represents linear regression and *R* is a correlation coefficient.

the radial profile of pressure. It has been found [*Lui and Hamilton*, 1992; *De Michelis et al.*, 1999] that in near-Earth region ($\mathbf{r} < 9\ R_E$) plasma pressure distribution can be described by power law dependence $P \propto \mathbf{r}^{-\alpha}$ with $\alpha \approx 3.3$. The plasma pressure values measured prior to dipolarization (at t_0) are plotted against geocentric distance in Figure 3a; here, the pressure obeys a power law dependence which is close to $P_0 \propto \mathbf{r}^{-4}$. This slope is steeper than that obtained by *Lui and Hamilton* [1992] for quiet time conditions, which can be attributed to the differences in distance ranges and activity levels in their data sets and ours. After dipolarization, the plasma pressure has the same slope but larger scatter (not shown). In the following, we correct the pressure value P_{DIP} for probe motion by normalizing it to r_0 distance as $P^*_{DIP} = P_{DIP}(r_{DIP}/r_0)^4$. Most of our events (135 of 147) happened on an outbound part of a probe orbit. Hence, on average P^*_{DIP}/P_0 is higher than P_{DIP}/P_0; the correction was <15% in 94% of events.

[27] Figure 3b shows the corrected ratio of postdipolarization plasma pressure to plasma pressure prior to dipolarization. The histogram peak (Figure 3c) is slightly above unity, which means that, on average, the plasma pressure distribution near the equatorial plane does not change dramatically after dipolarization. Although the scatter is large, on average the pressure increase during dipolarization is stronger close to Earth, whereas farther from Earth (at r = 10–12 R_E), the numbers of events with decreasing and increasing pressures are nearly equal, agreeing with the results of *Xing et al.* [2009]. It should be noted, however, that there is still an uncertainty with SST calibrations, and pressure values may be questionable in the near-Earth region where SST energies dominate.

[28] So far we have assumed that our measurements are made in the neutral sheet plane. In general, a field line passing through the probe maps it onto the neutral sheet surface at some larger distance. The difference in radial distance resulting from the equatorial projection is reduced when the magnetic configuration becomes more dipolar (when $|B_{xNS}/B_{zNS}|$ decreases). Hence, the postdipolarization observations are projected to closer radial distances than the predipolarization observations, and thus $P_{DIP}{}^*/P_0$ can be overestimated (under a nominal, monotonic pressure profile). This effect, which is expected to be more pronounced for the events observed farther from the neutral sheet plane, must vanish for the events at the neutral sheet. However, Figure 3d shows that $P_{DIP}{}^*/P_0$ seems to be even smaller for events having $|B_{xNS}/B_{zNS}| \sim 1$, demonstrating that field inclination changes have little effect on our results.

[29] We note that pressure often reaches its maximum during the period of turbulent *B* perturbation rather than at the end of the B_z growth phase (see Figure 1). We also computed the $P_{max}{}^*/P_0$ ratio and found that it ranges from 1 to ~2 with median 1.36 (not shown).

[30] Temperature and density changes are presented in Figures 3e and 3f. The density values were taken from ESA electron measurements. To filter out problematic density measurements, we required that $|n_i - n_e|/\langle n \rangle \leq 0.2$, which halved the number of events. Here n_e is density estimated

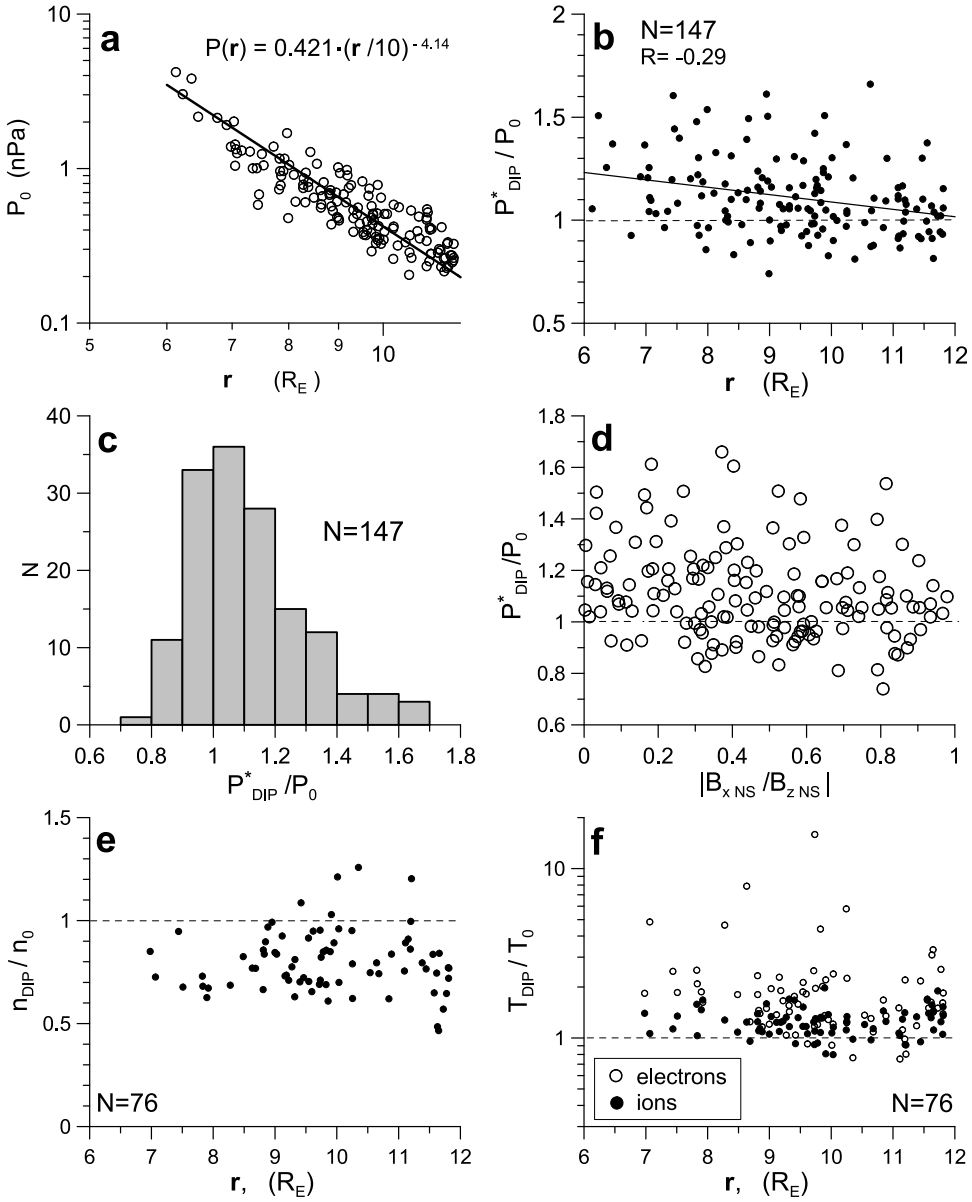

Figure 3. (a) Plasma pressure prior to the dipolarization as a function of geocentric distance (double logarithmic scale). The solid line represents regression and R is a correlation coefficient. (b) Ratio of the plasma pressure values after dipolarization to those before dipolarization versus geocentric distance of the probe location and (c) histogram of this ratio. (d) P^*_{DIP}/P_0, ratio of the measured pressure after dipolarization to the pressure before dipolarization as a function of the inverse tangent of magnetic field inclination prior to dipolarization. Zero values of B_{xNS}/B_{zNS} correspond to observations in the neutral sheet. (e) Ratio of the density values after dipolarization to those before dipolarization versus geocentric distance of the spacecraft location. (f) Ratio of the temperature values after dipolarization to those before dipolarization versus geocentric distance of the probe location. Open circles correspond to electron temperatures and closed circles correspond to ion temperatures. Note that temperature is presented on a logarithmic scale.

from the ESA electron detector, n_i is a sum of densities computed from ion ESA and SST detectors, and $\langle n \rangle = (n_i + n_e)/2$. Ion and electron temperatures were computed as $kT_i = P_i/n_e$ and $kT_e = P_e/n_e$, respectively. Density (Figure 3e) clearly decreased during dipolarization, whereas electron and ion temperatures increased (Figure 3f). The electron temperature (open circles) increased more strongly than ion temperature. In summary, the plasma in the postdipolarization region is hotter and more rarefied than that in the predipolarization region.

3. Entropy Changes

[31] Unlike the plasma pressure, the volume of the unit magnetic flux tube ($V = \int ds/B$) cannot be measured directly. Computation of the volume requires knowledge of the

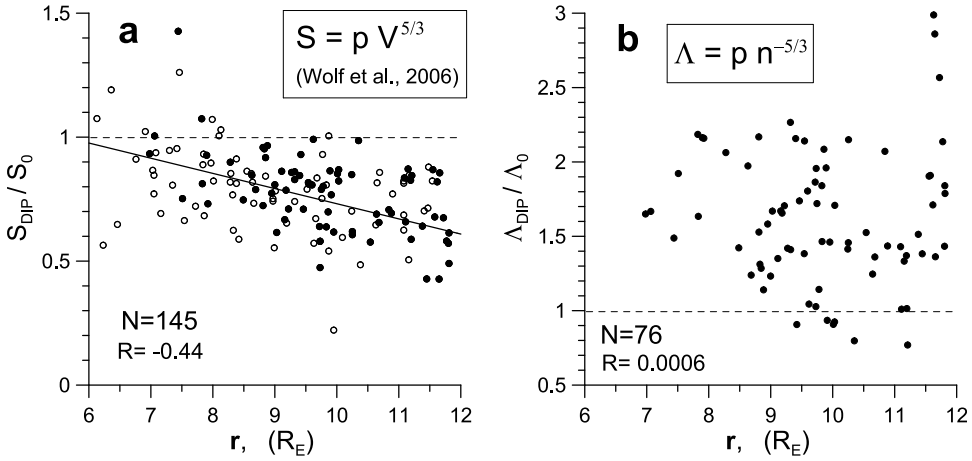

Figure 4. Ratio of entropy value after dipolarization to that before dipolarization versus radial distance. (a) Plasma tube entropy values were computed using the formula of *Wolf et al.* [2006]. Closed circles correspond to the points presented in Figure 4b. (b) Local entropy values $\Lambda = p/n^{5/3}$ were computed solely from local plasma measurements. The solid line represents regression and R is a correlation coefficient.

magnetic field distribution along the field line, so a single-point probe measurement alone cannot provide such information until the magnetic field model has been specified. In the plasma sheet the largest contribution to the flux tube volume comes from a near-equatorial region of small magnetic field, so the value of B_z^{NS} is the main controlling factor for V. In addition to B_z^{NS}, V depends on the "effective length" of the magnetic field line, which may experience large, complicated changes during the dipolarization.

[32] We use the formula for the unit magnetic flux tube volume suggested by *Wolf et al.* [2006], with some simple modifications applied. Starting from formulas describing V as a function of B_z, B_x, and pressure in the the 2-D pressure-balanced equilibrium magnetic configuration, these authors generalized the formulas by adding correction factors whose values have been obtained by fitting to a number of different pressure-balanced numerical magnetotail models. Their input parameters to compute V are the probe distance mapped onto the XY plane as well as observed plasma pressure and GSM B_r and B_z magnetic field components. (We assume that the flux tube volume does not depend on the presence of the azimuthal B-component [*Hau and Erickson*, 1995].) All results are obtained for zero dipole tilt angle. To take into account the dipole tilt effects, we used probe geocentric distance $r = (x^2 + y^2 + z^2)^{1/2}$ instead of $r = (x^2 + y^2)^{1/2}$ and the B_x, B_z magnetic field components in the NS frame rather than the GSM reference frame. The formula estimates the entropy on the field line crossing the magnetic equator beneath or above the probe.

[33] The results for the plasma tube entropy change in the course of dipolarization are shown in Figure 4a. We see that the entropy change increases with decreasing radial distance: the plasma tube entropy drops systematically toward 12 R_E, but the entropy changes on average approach zero toward 6 R_E.

[34] The S_{DIP}/S_0 ratio has not been corrected for the effect of probe motion. In average models the entropy is known to increase downtail and, since most of our events occur on the outbound part of the orbit, such correction would slightly decrease the S_{DIP}/S_0 values (our estimates indicate the correction must be within 10%).

[35] If pressure and density are not constant along a field line, the entropy definition presented in section 1 should be replaced with a more general one:

$$S^{3/5} = \int p^{3/5} dV = \int p^{3/5} \frac{dN}{n} = \int \Lambda^{3/5} dN. \qquad (2)$$

[36] Here, integration is performed along the flux tube, and N is the total number of particles inside the unit flux tube with volume V. This expression reveals the relation between the entropy S and local entropy of a flux tube element $\Lambda = pn^{-5/3}$. If pressure and density are constant along the field line, the two entropy estimates are scaled as $S = \Lambda N^{5/3}$. If N does not vary in space and is conserved in time, both spatial and temporal variations of the two quantities would correlate. Comparing Figures 4a and 4b, however, we see very different behaviors of the two entropy parameters. We could estimate the net change of the total particle content from our data sets as $N_{DIP}/N_0 = (S_{DIP}/S_0)^{3/5}/(\Lambda_{DIP}/\Lambda_0)^{3/5}$. According to Figure 5, N shows a large drop after dipolarization (the median N_{DIP}/N_0 is 0.63), demonstrating ~40% reduction in flux tube content without obvious dependence upon the radial distance.

[37] As can be seen in Figure 1 and in more than half of the events, the pressure actually starts to increase for tens of seconds to a few minutes prior to sharp dipolarization onset in the magnetic field. The plasma changes characterizing this precursor are illustrated in Figure 6a, which shows the ratio of pressure just prior to B_z onset (subscript 0D) to pressure before the start of pressure growth (subscript 0). Comparison with Figure 3b demonstrates that the amount of pressure increase during this precursor phase is comparable to (or perhaps even higher than) the postdipolarization pressure increase.

[38] As opposed to the postdipolarization state, average entropy does not change during this period (Figure 6b, with the exception of a few events mostly closest to Earth). The

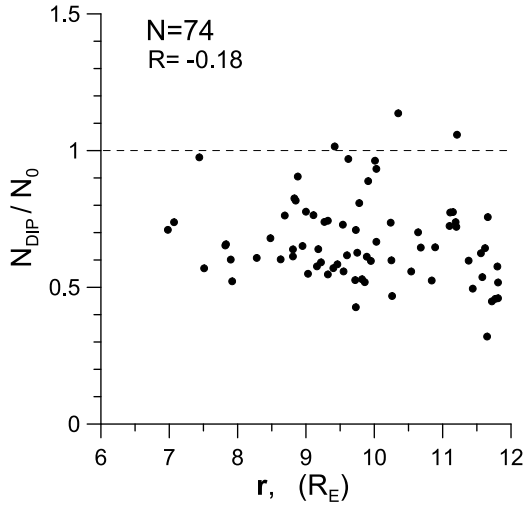

Figure 5. Ratio of the number of particles in unit flux tube after dipolarization to that before dipolarization versus geocentric distance of the probe location. *R* is a correlation coefficient.

same conclusion is supported by the local entropy estimates (Figure 6c). In conclusion, the plasma changes during this precursor phase resemble adiabatic compression, which is very different from the situation during the dipolarization period.

[39] It should be noted that the duration of the precursor phase is less or on the order of the transition time needed for the configuration to achieve equilibrium. Therefore, the results based on plasma measurements at t_{0D} can be affected by the plasma dynamics along a flux tube.

4. Discussion and Concluding Remarks

[40] Our analysis suggests that, ignoring complicated variations during the nonstationary turbulent dipolarization process, large-scale plasma parameter changes associated with the dipolarization can be separated into two types. The first is adiabatic compression of the plasma, a type of compression wave preceding dipolarization. This effect is closely associated with the initial plasma flow increase (see *Sergeev et al.* [1996, 2009] and statistics in the work of *Ohtani et al.* [2004]). Compression has been observed consistently with corresponding time delays on multiple, radially separated THEMIS probes [*Runov et al.*, 2009; *Sergeev et al.*, 2009]. This suggests that a sheathlike spatial structure develops ahead of the Earthward propagating dipolarization front and is responsible for the adiabatic compression. The amplitude of this compression (Figure 6a) might be comparable to that of the postdipolarization pressure increase (Figure 3b). Our analysis shows that this compression is indeed adiabatic (Figures 6b and 6c). This feature was also reproduced in recent RCM simulations of bubble propagation [*Zhang et al.*, 2009].

[41] The second type is evidenced by properties of postdipolarization plasma: it consists of heated but diluted plasma. The entropy of this hot, dilute plasma (Figures 3e and 3f) is different from that of undisturbed predipolarization plasma (Figure 4a). Thus, plasma tubes with lower entropy and reduced particle content (Figure 5) replace the original plasma tubes. We interpret this exchange as the arrival of plasma sheet tubes with reduced entropy: the bubbles.

[42] The plasma pressure does not change dramatically. In 92% of events, P^*_{DIP}/P_0 was in the range 0.8–1.4 with median 1.08, demonstrating the tendency of plasma pressure to increase during dipolarization. This increase is more pronounced in the near-Earth region at $r < 10\ R_E$. The results presented in Figure 3b agree with those obtained by *Kistler et al.* [1992], who studied the total pressure variations based on Active Magnetospheric Particle Tracer Explorers mea-

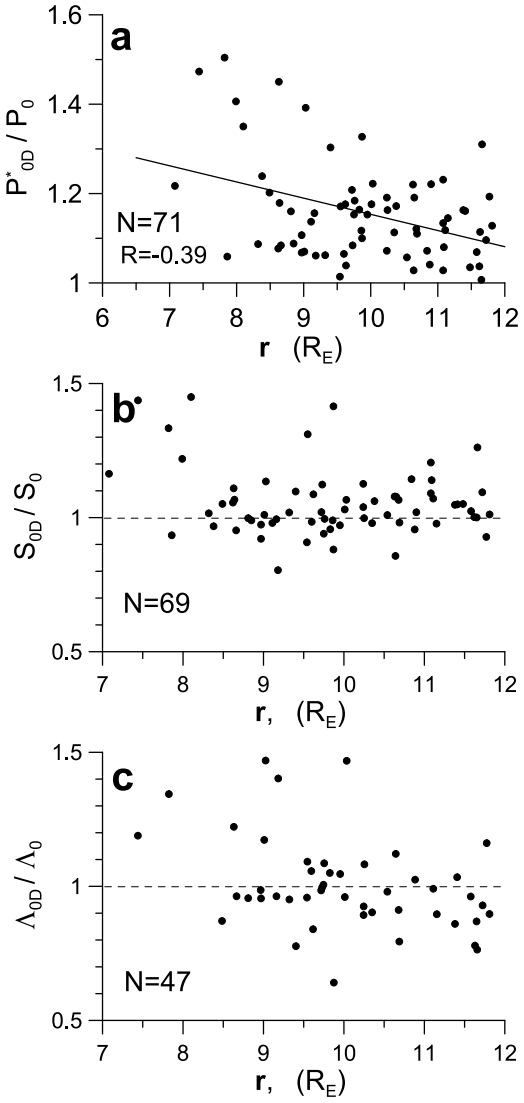

Figure 6. (a) Ratio of the plasma pressure values at the end of the predipolarization phase to those before any precursor of dipolarization versus geocentric distance of the probe location. The solid line represents regression and *R* is a correlation coefficient. (b) Ratio of $S = pV^{5/3}$ value at the end of the predipolarization phase to that before any precursor of dipolarization versus radial distance. The value of $pV^{5/3}$ was estimated from the formulas of *Wolf et al.* [2006]. (c) The ratio of the $\Lambda = pn^{-5/3}$ value at the end of the predipolarization phase to that before any precursor of dipolarization versus radial distance.

surements as well as those of *Miyashita et al.* [2009], who found particle pressure increase in the near-Earth region associated with substorm onset. Our results also agree with the conclusions of *Xing et al.* [2009], who found plasma pressure increase at $r < 12\ R_E$ and decrease at $r > 16\ R_E$. They differ, however, from the results of *Lyons et al.* [2003], most likely because the authors did not include the energetic particles in their analysis.

[43] We computed the entropy of a plasma tube from single probe measurements applying the formula of *Wolf et al.* [2006]. It can be concluded that entropy decreases at $r > 10\ R_E$, whereas its change goes to zero, or even may be slightly positive in the near-Earth region, near geostationary orbit. We suggest that entropy changes for every particular event depend on r in the same manner as average changes do.

[44] To interpret these results in terms of bubble theory, we should consider the processes that begin when a bubble stops in the near-Earth region. The MHD simulations of *Chen and Wolf* [1999] show that the bubble stops at the point where its own entropy is equal to that of the surrounding flux tubes. In this case, the single, small-scale bubble will not change entropy distribution at all. Dipolarization is a large-scale phenomenon, however, that should involve multiple bubbles in a finite volume. Suggesting two-dimensionality as a first approximation, we can speculate that when a bubble reaches the region occupied by flux tubes with the same entropy, it stops in front of them, pushing the tubes with higher entropy downtail because of interchange instability. As a new bubbles come from the magnetotail, a tailward propagating region of low entropy is formed. This scenario is consistent with our findings: the entropy decrease is stronger farther from Earth (Figures 3b and 4a). At this simplified level of reasoning, we do not see any contradictions between the bubble scenario and observations. However, in our speculation we oversimplified the physics. In fact, in the near-Earth region both magnetic drifts and losses through precipitation remove hot particles from the bubble. Further theoretical studies of the final stage of bubble evolution, including kinetic effects, are necessary to better understand the physics of dipolarization fronts.

[45] The reduction in flux tube content N_{DIP}/N_0 (Figure 5) does not demonstrate any clear dependence on r, suggesting that the process responsible for this reduction operates outside $r = 12\ R_E$ rather than in the near-Earth region.

[46] Otherwise, one might expect to see a steplike drop at the sink location or gradual reduction toward the Earth in the case of continuously operating mechanisms like loss cone precipitation or magnetic drifts.

[47] We summarize our experimental findings concerning dipolarizations in the region $r = 6$–$12\ R_E$ as follows:

[48] 1. Dipolarization occurs in two stages: adiabatic and laminar compression in front of the propagating dipolarization front and arrival of the bubble or flux tube with reduced entropy.

[49] 2. The particle content of the postdipolarization flux tubes is reduced by ~40% over that of the undisturbed (predipolarization) tubes.

[50] 3. The mechanism responsible for bubble entropy reduction operates outside $r = 12\ R_E$.

[51] 4. On average, the plasma pressure changes very little at $r = 10$–$12\ R_E$ and increases only slightly in the near-Earth region.

[52] 5. The value of $pn^{-5/3}$ shows significant increase after dipolarization.

[53] **Acknowledgments.** We acknowledge NASA contracts NNX08AD85G and NAS5-02099, the German Ministry for Economy and Technology, and the German Center for Aviation and Space (DLR), contract 50 OC 0302. The work by S.D., V.S., and S.A. was supported by Russian Ministry of Education and Science grants, by CRDF grant RUG1-2861-ST-07, and by RFBR grants 10-05-91163 and 10-05-00223. We thank Judy Hohl for help with manuscript preparation.

[54] Masaki Fujimoto thanks the reviewers for their assistance in evaluating this paper.

References

Angelopoulos, V., C. F. Kennel, F. V. Coroniti, R. Pellat, M. G. Kivelson, R. J. Walker, C. T. Russell, W. Baumjohann, W. C. Feldman, and J. T. Gosling (1994), Statistical characteristics of bursty bulk flow events, *J. Geophys. Res.*, *99*(A11), 21,257–21,280.

Auster, H. U., et al. (2008), The THEMIS fluxgate magnetometer, *Space Sci. Rev.*, *141*, 235–264, doi:10.1007/s11214-008-9365-9.

Baker, D. N., T. I. Pulkkinen, V. Angelopoulos, W. Baumjohann, and R. L. McPherron (1996), Neutral line model of substorms: Past results and present view, *J. Geophys. Res.*, *101*(A6), 12,975–13,010.

Baumjohann, W. (1993), The near Earth plasma sheet—An AMPTE/IRM perspective, *Space Sci. Rev.*, *64*(1–2), 141–163.

Baumjohann, W., G. Paschmann, and H. Lühr (1990), Characteristics of high-speed ion flows in the plasma sheet, *J. Geophys. Res.*, *95*(A4), 3801–3809.

Birn, J., M. Hesse, and K. Schindler (1996), MHD simulations of magnetotail dynamics, *J. Geophys. Res.*, *101*(A6), 12,939–12,954.

Birn, J., J. Raeder, Y. L. Wang, R. A. Wolf, and M. Hesse (2004), On the propagation of bubbles in the geomagnetic tail, *Ann. Geophys.*, *22*, 1773–1786.

Birn, J., M. Hesse, K. Schindler, and S. Zaharia (2009), Role of entropy in magnetotail dynamics, *J. Geophys. Res.*, *114*, A00D03, doi:10.1029/2008JA014015.

Bonnell, J. W., F. S. Mozer, G. T. Delory, A. J. Hull, R. E. Ergun, C. M. Cully, V. Angelopoulos, and P. R. Harvey (2008), The Electric Field Instrument (EFI) for THEMIS, *Space Sci. Rev.*, *141*, 303–341.

Chen, C. X., and R. A. Wolf (1999), Theory of thin-filament motion in Earth's magnetotail and its application to bursty bulk flows, *J. Geophys. Res.*, *104*(A7), 14,613–14,626.

De Michelis, P., I. A. Daglis, and G. Consolini (1999), An average image of proton plasma pressure and of current systems in the equatorial plane derived from AMPTE/CCE-CHEM measurements, *J. Geophys. Res.*, *104*(A12), 28,615–28,624.

Erickson, G. M., and R. A. Wolf (1980), Is steady convection possible in the Earth's magnetotail?, *Geophys. Res. Lett.*, *7*(11), 897–900.

Hau, L.-N., and G. M. Erickson (1995), Penetration of the interplanetary magnetic field by into Earth's plasma sheet, *J. Geophys. Res.*, *100*(A11), 21,745–21,751.

Jacquey, C., J. A. Sauvaud, and J. Dandouras (1991), Location and propagation of the magnetotail substorm expansion: Analysis and simulation of an ISEE multi-onset event, *Geophys. Res. Lett.*, *18*(3), 389–392.

Jacquey, C., J. A. Sauvaud, J. Dandouras, and A. Korth (1993), Tailward propagating tail current disruption and dynamics of the near-Earth tail: A multi-point measurement anaysis, *Geophys. Res. Lett.*, *20*(10), 983–986.

Kistler, L. M., E. Möbius, W. Baumjohann, G. Paschmann, and D. C. Hamilton (1992), Pressure changes in the plasma sheet during substorm injections, *J. Geophys. Res.*, *97*(A3), 2973–2983.

Lemon, C., R. A. Wolf, T. W. Hill, S. Sazykin, R. W. Spiro, F. R. Toffoletto, J. Birn, and M. Hesse (2004), Magnetic storm ring current injection modeled with the Rice Convection Model and a self-consistent magnetic field, *Geophys. Res. Lett.*, *31*, L21801, doi:10.1029/2004GL020914.

Lopez, R. E., and A. T. Y. Lui (1990), A multisatellite case study of the expansion of a substorm current wedge in the near-Earth magnetotail, *J. Geophys. Res.*, *95*(A6), 8009–8017.

Lui, A. T. Y. (1996), Current disruption in the Earth's magnetosphere: Observations and models, *J. Geophys. Res.*, *101*(A6), 13,067–13,088.

Lui, A. T. Y., and D. C. Hamilton (1992), Radial profiles of quiet time magnetospheric parameters, *J. Geophys. Res.*, *97*(A12), 19,325–19,332.

Lui, A. T. Y., R. Lopez, B. Anderson, K. Takahashi, L. Zanetti, R. McEntire, T. Potemra, D. Klumpar, E. Greene, and R. Strangeway (1992), Current disruptions in the near-Earth neutral sheet region, *J. Geophys. Res.*, *97*(A2), 1461–1480.

Lui, A. T. Y., K. Liou, P. T. Newell, C.-I. Meng, S.-I. Ohtani, T. Ogino, S. Kokubun, M. J. Brittnacher, and G. K. Parks (1998), Plasma and magnetic flux transport associated with auroral breakups, *Geophys. Res. Lett.*, *25*(21), 4059–4062.

Lyons, L. R., C.-P. Wang, T. Nagai, T. Mukai, Y. Saito, and J. C. Samson (2003), Substorm inner plasma sheet particle reduction, *J. Geophys. Res.*, *108*(A12), 1426, doi:10.1029/2003JA010177.

McFadden, J. P., C. W. Carlson, D. Larson, V. Angelopoulos, M. Ludlam, R. Abiad, B. Elliott, P. Turin, and M. Marckwordt (2008), The THEMIS ESA plasma instrument and in-flight calibration, *Space Sci. Rev.*, *141*, 277–302, doi:10.1007/s11214-008-9440-2.

McPherron, R. L., C. T. Russell, and M. P. Aubry (1973), Satellite studies of magnetosphereic substorms on August 15, 1968: 9. Phenomenological model of substorms, *J. Geophys. Res.*, *78*(16), 3131–3149.

Miyashita, Y., S. Machida, T. Mukai, Y. Saito, K. Tsuruda, H. Hayakawa, and P. R. Sutcliffe (2000), A statistical study of variations in the near and middistant magnetotail associated with ssubstorm onsets: Geotail observations, *J. Geophys. Res.*, *105*(A7), 15,913–15,930.

Miyashita, Y., et al. (2009), A state-of-the-art picture of substorm-associated evolution of the near-Earth magnetotail obtained from superposed epoch analysis, *J. Geophys. Res.*, *114*, A01211, doi:10.1029/2008JA013225.

Nagai, T., M. Fujimoto, Y. Saito, S. Machida, T. Terasawa, R. Nakamura, T. Yamamoto, T. Mukai, A. Nishida, and S. Kokubun (1998), Structure and dynamics of magnetic reconnection for substorm onsets with Geotail observations, *J. Geophys. Res.*, *103*(A3), 4419–4440.

Nakamura, R., W. Baumjohann, M. Brittnacher, V. A. Sergeev, M. Kubyshkina, T. Mukai, and K. Liou (2001), Flow bursts and auroral activations: Onset timing and foot point location, *J. Geophys. Res.*, *106*(A6), 10,777–10,789.

Ohtani, S., S. Kokubun, and C. T. Russell (1992), Radial expansion of the tail current disruption during substorm: A new approach to the substorm onset region, *J. Geophys. Res.*, *97*(A3), 3129–3136.

Ohtani, S. I., M. A. Shay, and T. Mukai (2004), Temporal structure of the fast convective flow in the plasma sheet: Comparison between observations and two-fluid simulations, *J. Geophys. Res.*, *109*, A03210, doi:10.1029/2003JA010002.

Pontius, D. H., and A. Wolf (1990), Transient flux tubes in the terrestrial magnetosphere, *Geophys. Res. Lett.*, *17*(1), 49–52.

Runov, A., V. Angelopoulos, M. I. Sitnov, V. A. Sergeev, J. Bonnell, J. P. McFadden, D. Larson, K.-H. Glassmeier, and U. Auster (2009), THEMIS observations of an earthward-propagating dipolarization front, *Geophys. Res. Lett.*, *36*, L14106, doi:10.1029/2009GL038980.

Sergeev, V. A., V. Angelopoulos, J. T. Gosling, C. A. Cattell, and C. T. Russell (1996), Detection of localized, plasma-depleted flux tubes or bubbles in the midtail plasma sheet, *J. Geophys. Res.*, *101*(A5), 10,817–10,826.

Sergeev, V., V. Angelopoulos, S. Apatenkov, J. Bonnell, R. Ergun, R. Nakamura, J. McFadden, D. Larson, and A. Runov (2009), Kinetic structure of the sharp injection/dipolarization front in the flow-braking region, *Geophys. Res. Lett.*, *36*, L21105, doi:10.1029/2009GL040658.

Shiokawa, K., et al. (1998), High-speed ion flow, substorm current wedge, and multiple Pi 2 pulsations, *J. Geophys. Res.*, *103*(A3), 4491–4507.

Takada, T., R. Nakamura, W. Baumjohann, Y. Asano, M. Volwerk, T. L. Zhang, B. Klecker, H. Rème, E. A. Lucek, and C. Carr (2006), Do BBFs contribute to inner magnetosphere dipolarizations: Concurrent Cluster and Double Star observations, *Geophys. Res. Lett.*, *33*, L21109, doi:10.1029/2006GL027440.

Tsyganenko, N. A., and D. H. Fairfield (2004), Global shape of the magnetotail current sheet as derived from Geotail and Polar data, *J. Geophys. Res.*, *109*, A03218, doi:10.1029/2003JA010062.

Wolf, R. A., V. Kumar, F. R. Toffoletto, G. M. Erickson, A. M. Savoie, C. X. Chen, and C. L. Lemon (2006), Estimating local plasma sheet $PV^{5/3}$ from single-spacecraft measurements, *J. Geophys. Res.*, *111*, A12218, doi:10.1029/2006JA012010.

Wolf, R. A., Y. Wan, X. Xing, J.-C. Zhang, and S. Sazykin (2009), Entropy and plasma sheet transport, *J. Geophys. Res.*, *114*, A00D05, doi:10.1029/2009JA014044.

Xing, X., L. R. Lyons, V. Angelopoulos, D. Larson, J. McFadden, C. Carlson, A. Runov, and U. Auster (2009), Plasma sheet pressure evolution related to substorms, *J. Geophys. Res.*, *115*, A01212, doi:10.1029/2009JA014315.

Zhang, J.-C., R. A. Wolf, R. W. Spiro, G. M. Erickson, S. Sazykin, F. R. Toffoletto, and J. Yang (2009), Rice Convection Model simulation of the substorm-associated injection of an observed plasma bubble into the inner magnetosphere: 2. Simulation results, *J. Geophys. Res.*, *114*, A08219, doi:10.1029/2009JA014131.

V. Angelopoulos, Institute of Geophysics and Planetary Physics, University of California, Los Angeles, CA 90095, USA.

S. V. Apatenkov, S. Dubyagin, and V. Sergeev, Earth Physics Department, St. Petersburg State University, Ulyanovskaya 1, Petrodvoretz, St. Petersburg 198504, Russia. (stepan@geo.phys.spbu.ru)

J. W. Bonnell, D. Larson, and J. P. McFadden, Space Sciences Laboratory, University of California, 7 Gauss Way, Berkeley, CA 94720, USA.

R. Nakamura, Space Research Institute, Austrian Academy of Sciences, Schmiedlstr. 6, A-8042 Graz, Austria.